nature water

Supplementary information

https://doi.org/10.1038/s44221-024-00251-4

Decarbonization potential of floating solar photovoltaics on lakes worldwide

In the format provided by the authors and unedited

Supplementary Information

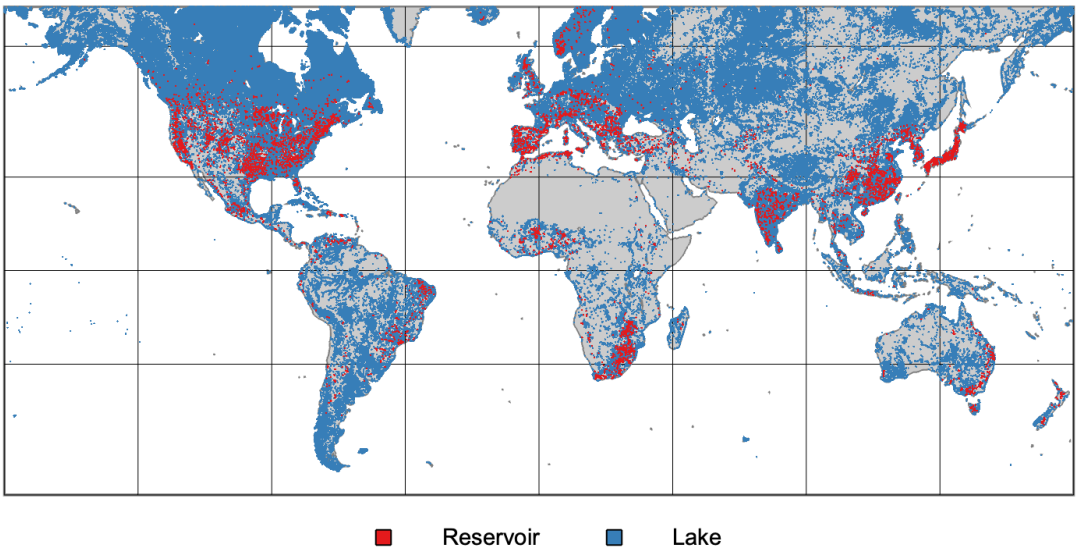

Supplementary Figure 1 | The location of each water body included in this study.

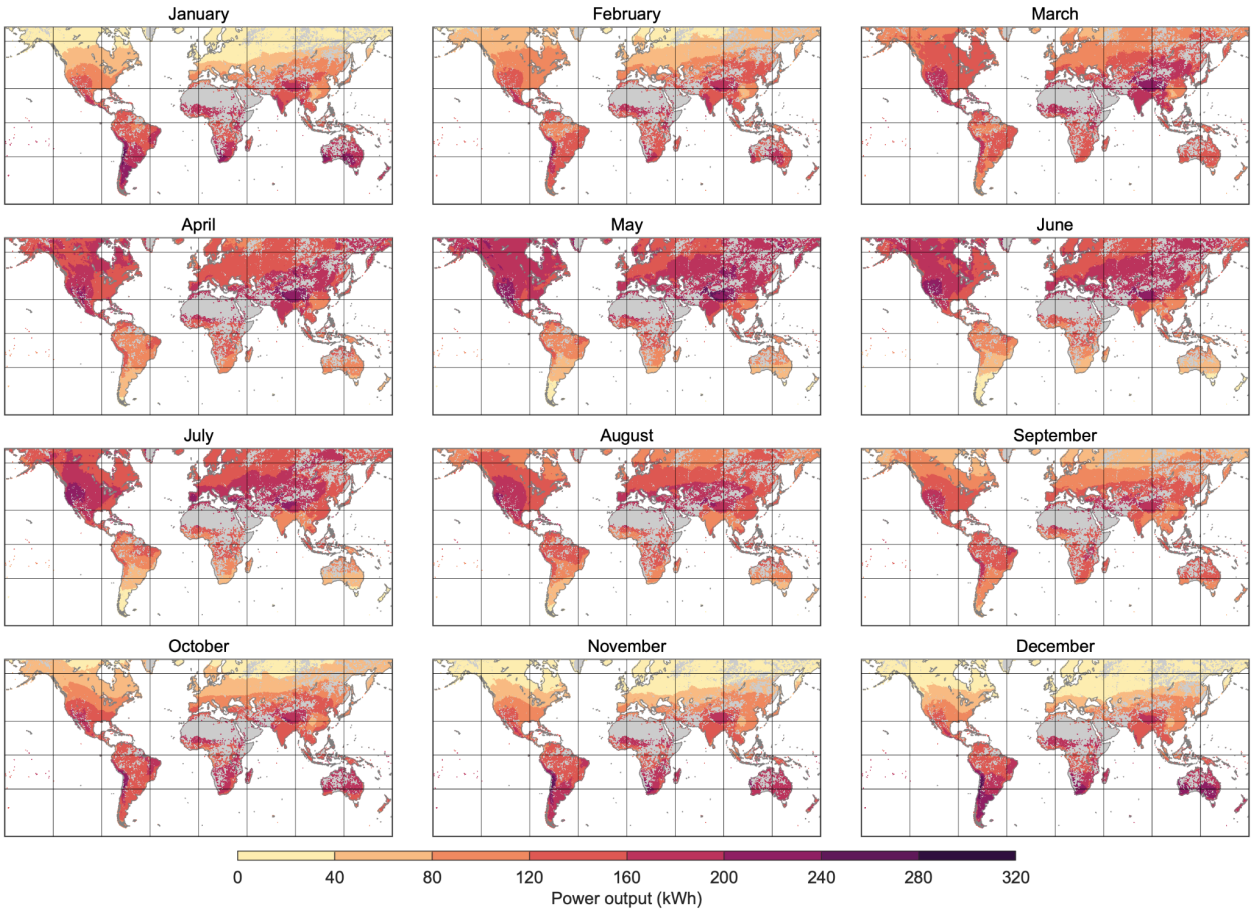

Supplementary Figure 2 | Seasonal variations in the simulated annual power output of a 1-kW FPV system in each of the studied water bodies. The power output from a 1-kW FPV was initially calculated at hourly intervals, and then summed at monthly scales over the period 1991-2020.

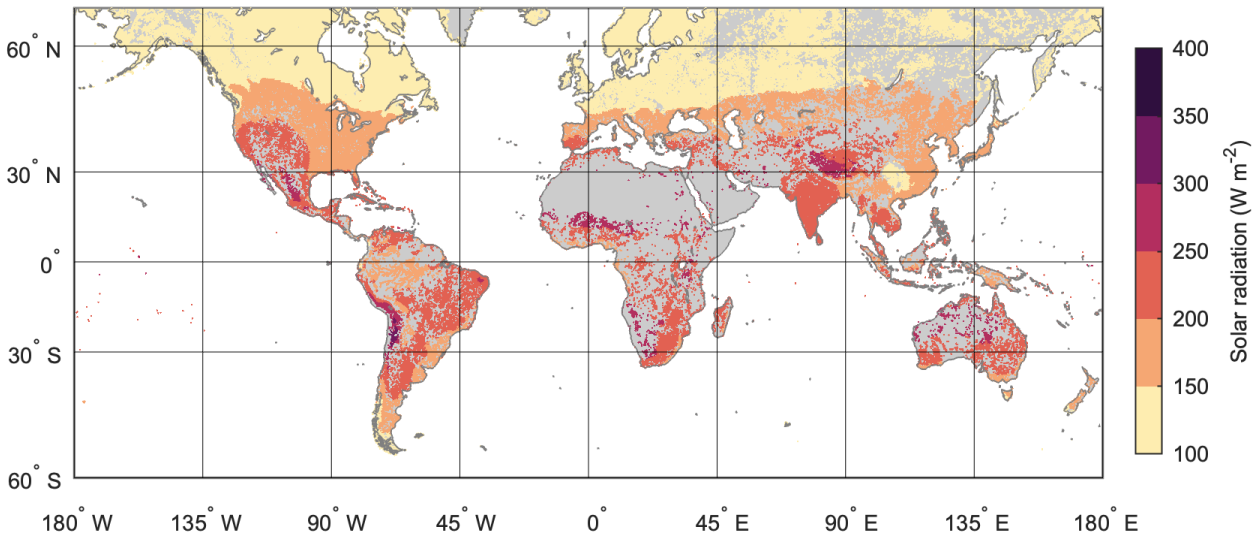

Supplementary Figure 3 | Global variations in annual average incoming solar radiation at the location of each of the water bodies included in this study. Solar radiation data were downloaded from ERA5.

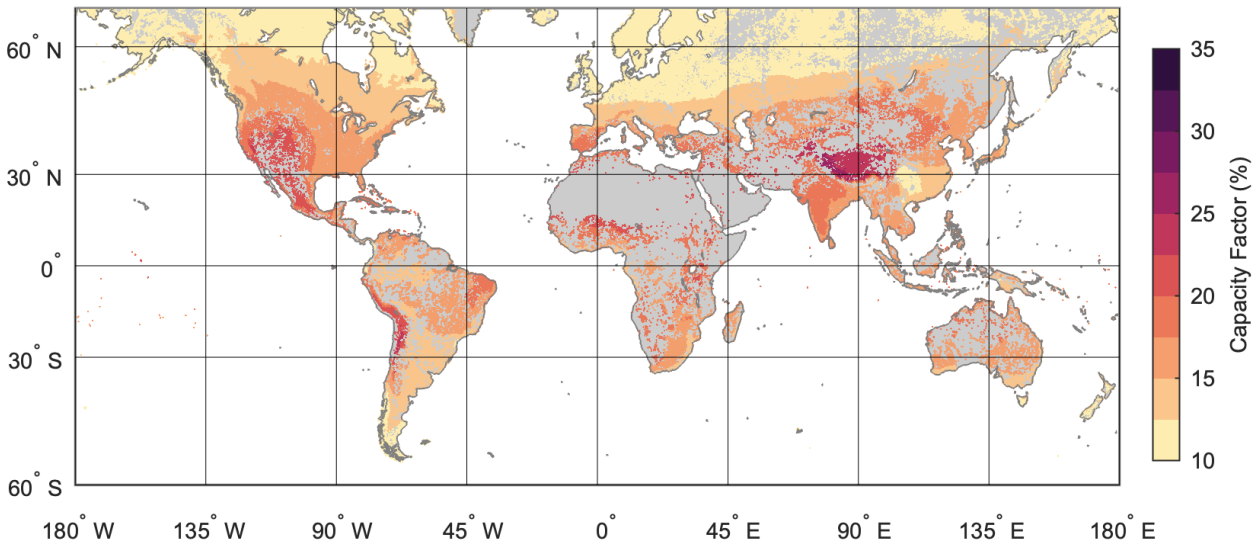

Supplementary Figure 4 | Global variations in the simulated annual capacity factor in each of the studied water bodies over the period 1991-2020.

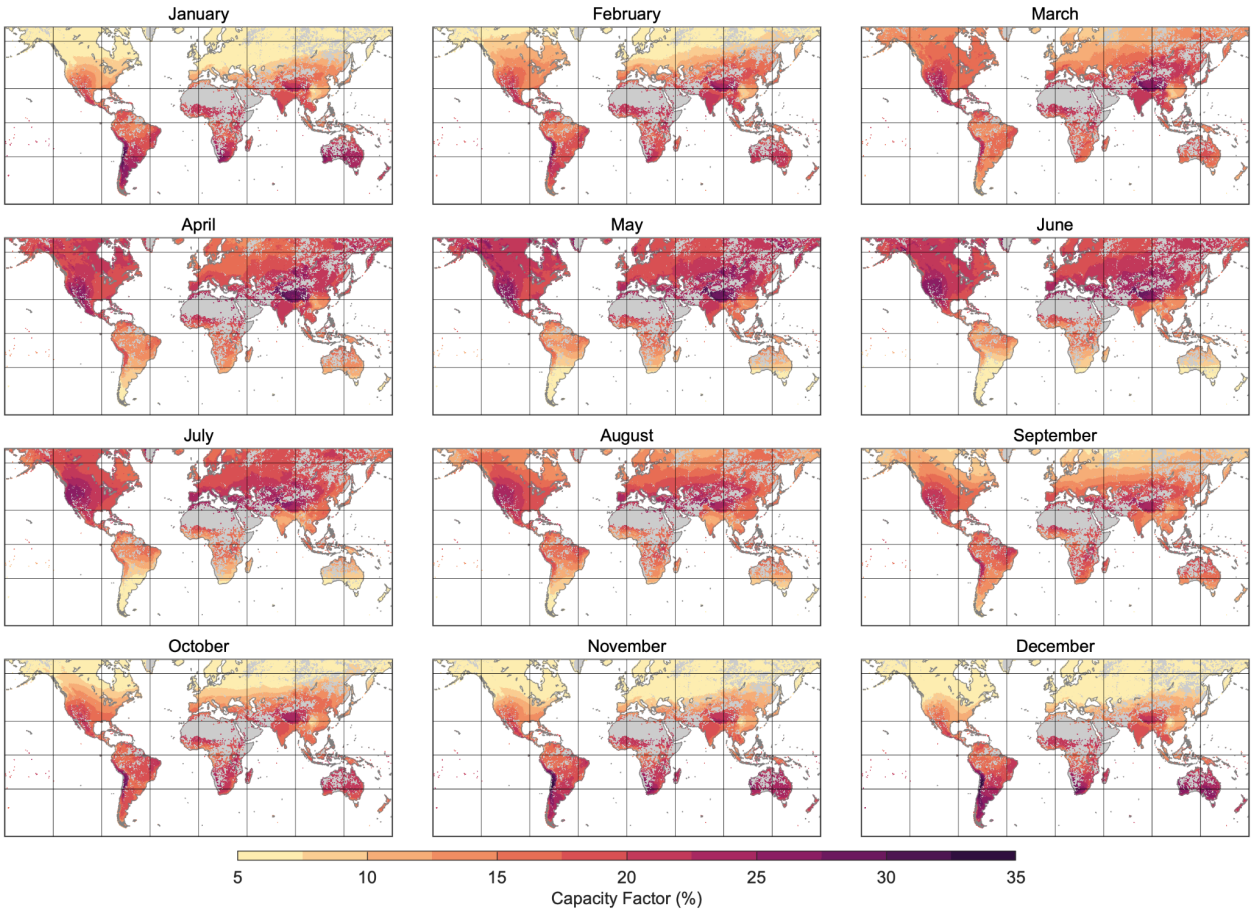

Supplementary Figure 5 | Seasonal variations in the simulated capacity factor in each of the studied water bodies, averaged over the period 1991-2020.

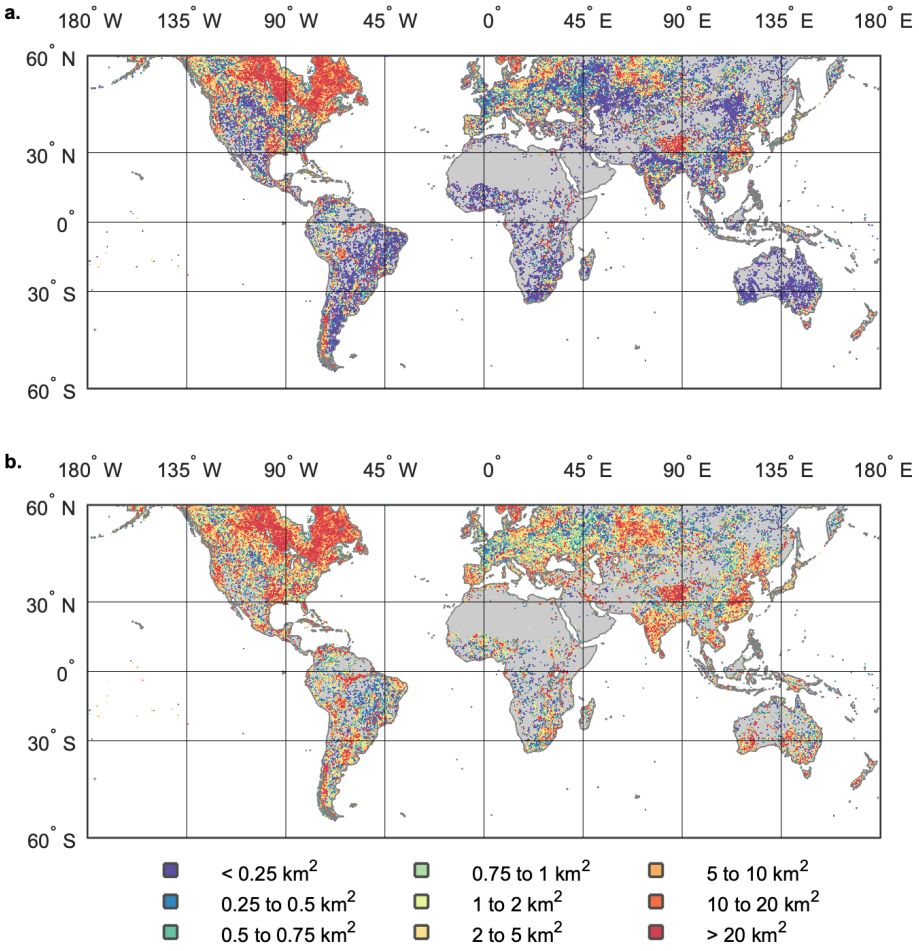

Supplementary Figure 6 | Shown are variations in water body surface area across all studied sites from 1991-2020. Specifically, we show the (**a**) Minimum and (**b**) Maximum water body surface area.

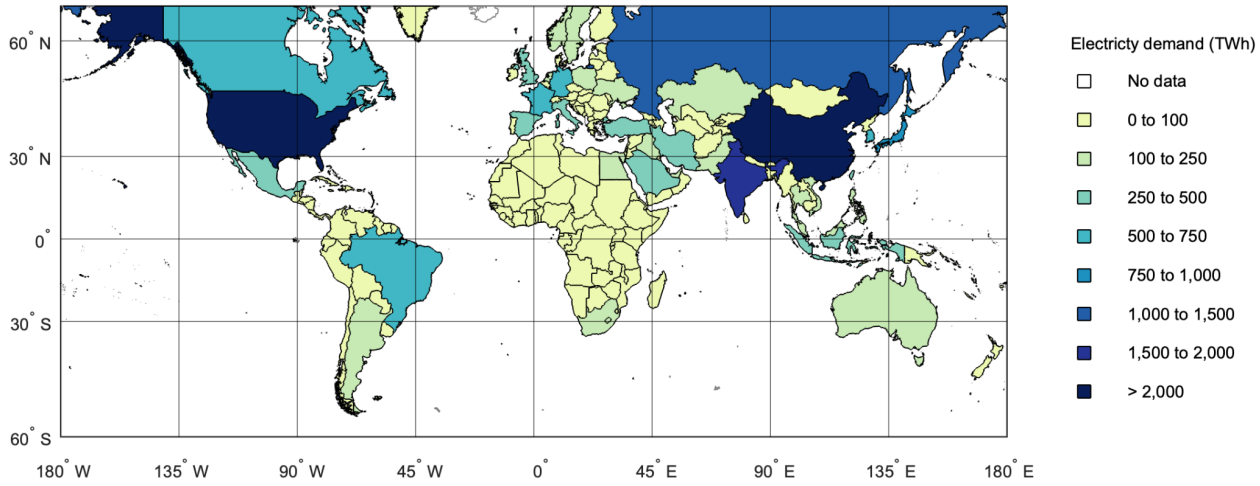

Supplementary Figure 7 | Annual electricity demand per country in 2021. Electricity demand is described as total electricity generation, adjusted for electricity imports and exports.

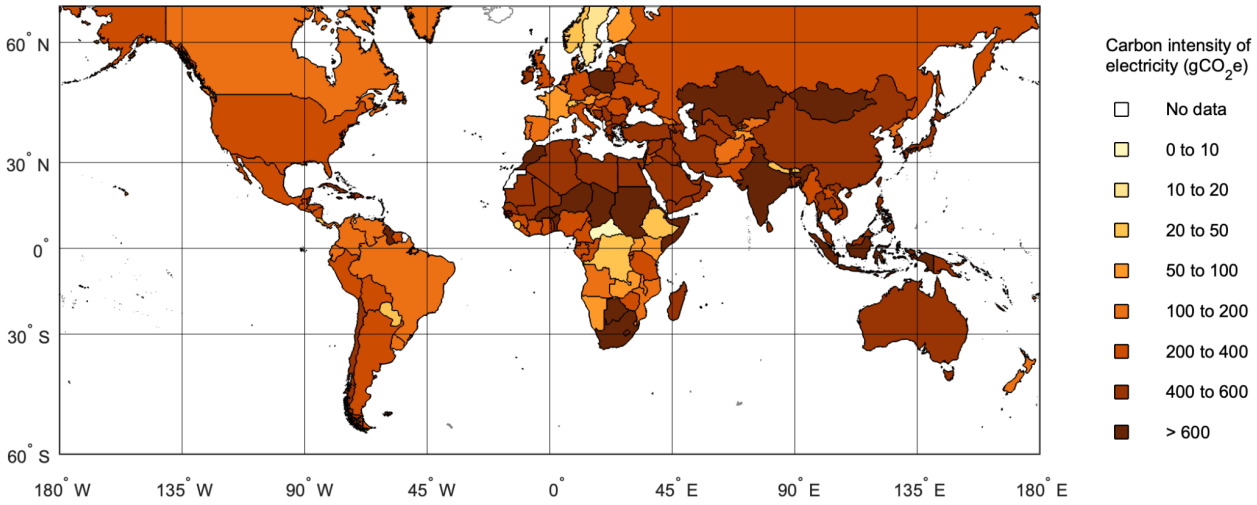

Supplementary Figure 8 | Carbon intensity of electricity in 2021. Carbon intensity is measured in grams of carbon dioxide-equivalents emitted per kilowatt-hour of electricity.

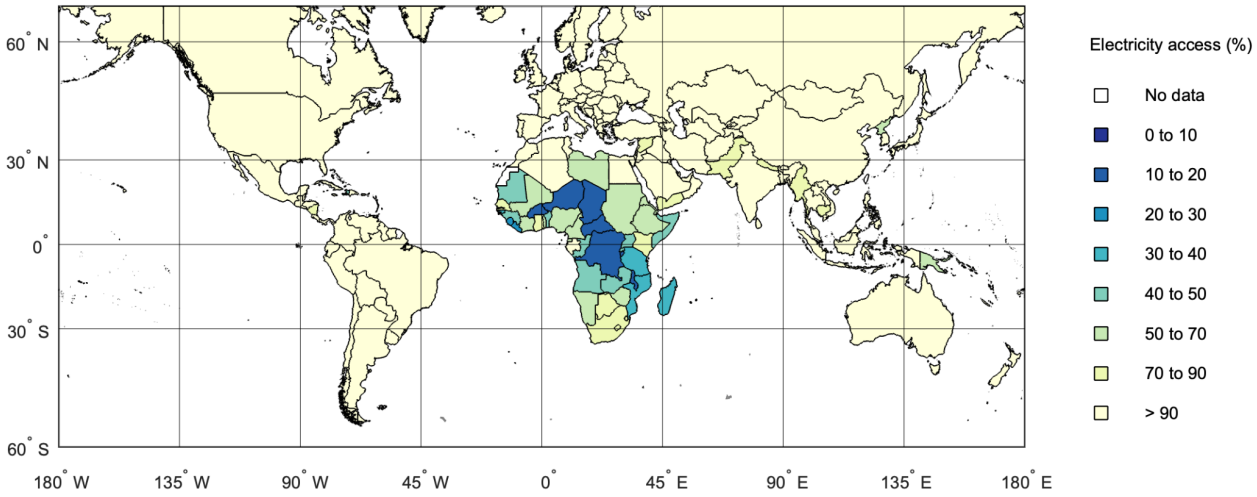

Supplementary Figure 9 | Percentage of the population with access to electricity in 2020 (the latest year with available data).

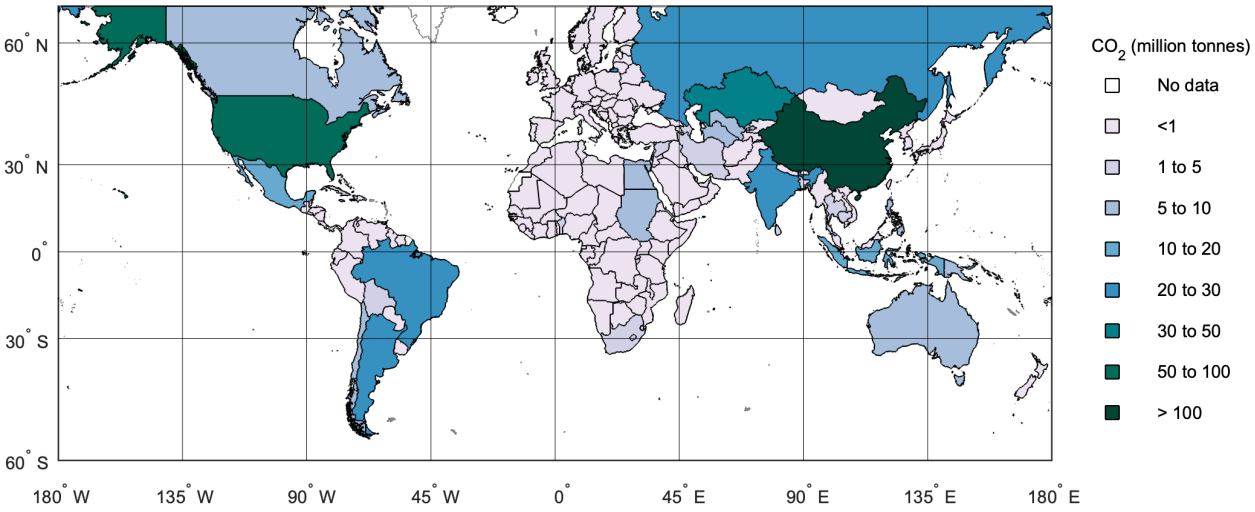

Supplementary Figure 10 | Potential reduction in CO_2 emissions per country following the deployment of FPV systems.

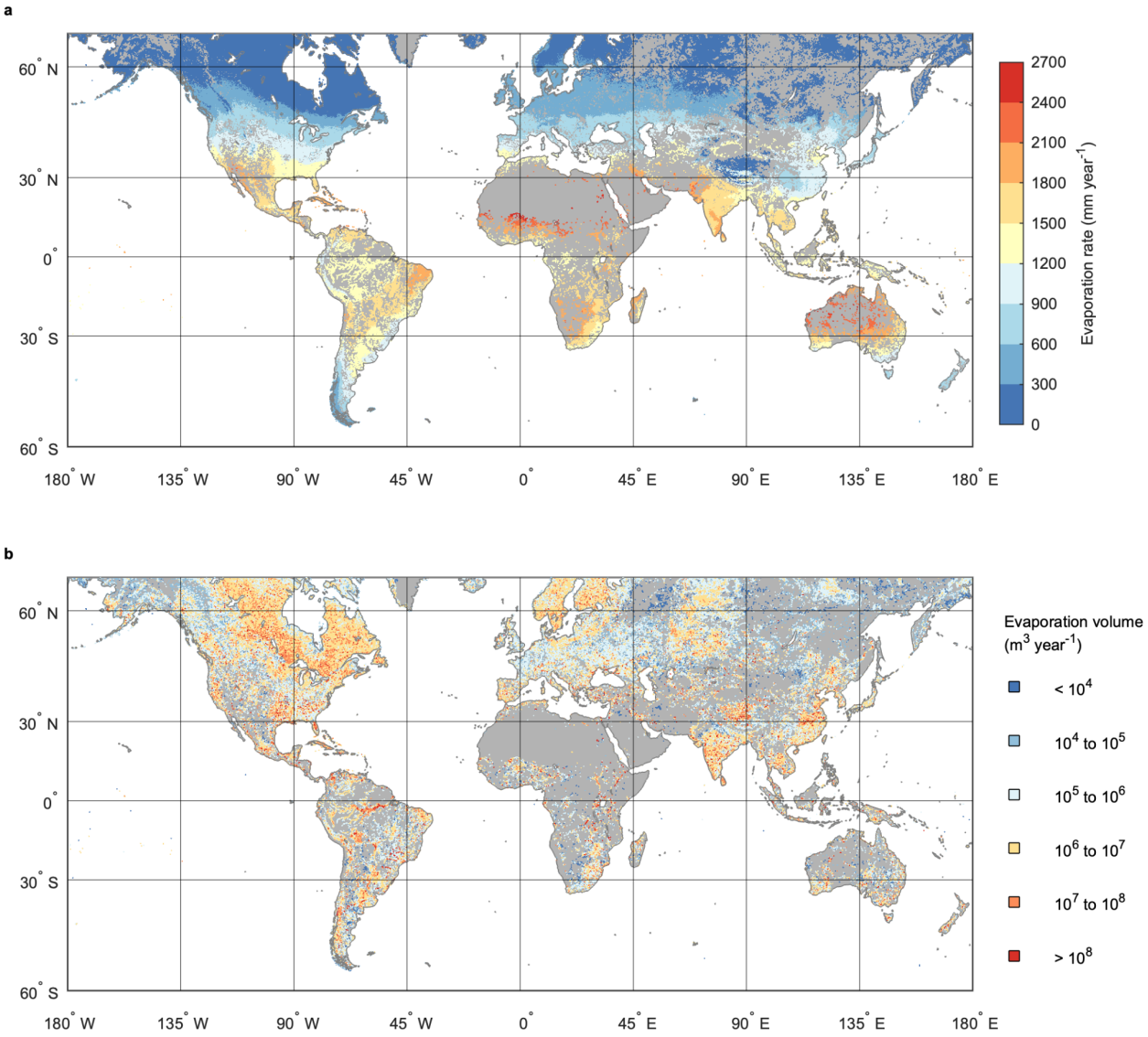

Supplementary Figure 11 | Annual (**a**) evaporation rate, and (**b**) evaporation volume for each studied water body, averaged over the study period (1991-2020).

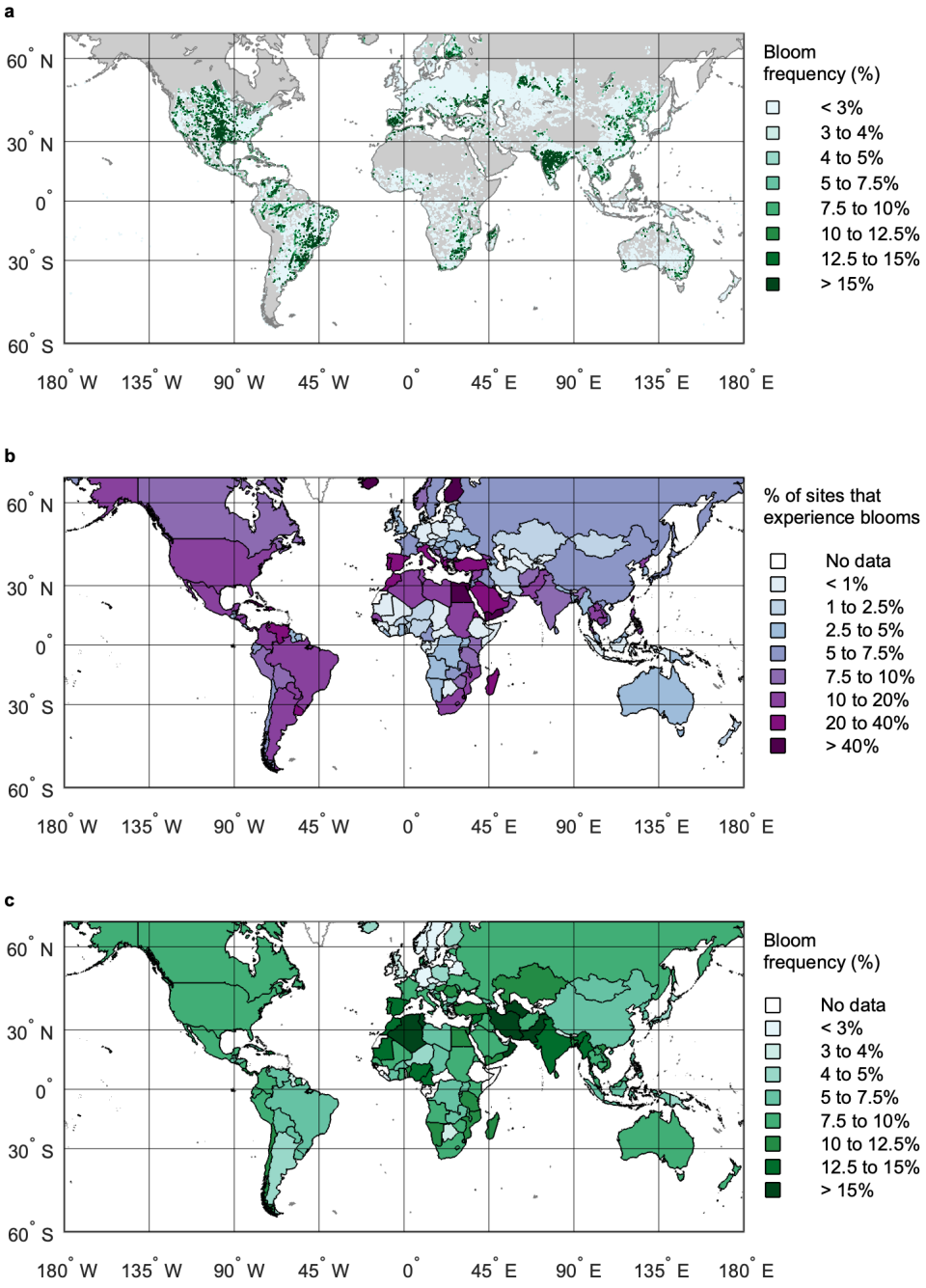

Supplementary Figure 12 | Water-body-specific and national-scale summaries of algal bloom occurrence. Shown are (**a**) the frequency of algal blooms in 236,913 water bodies worldwide; (**b**) the percentage of water bodies in each country that have experienced at least one algal bloom between 1982 and 2019; (**c**) national-scale average frequency of algal blooms.

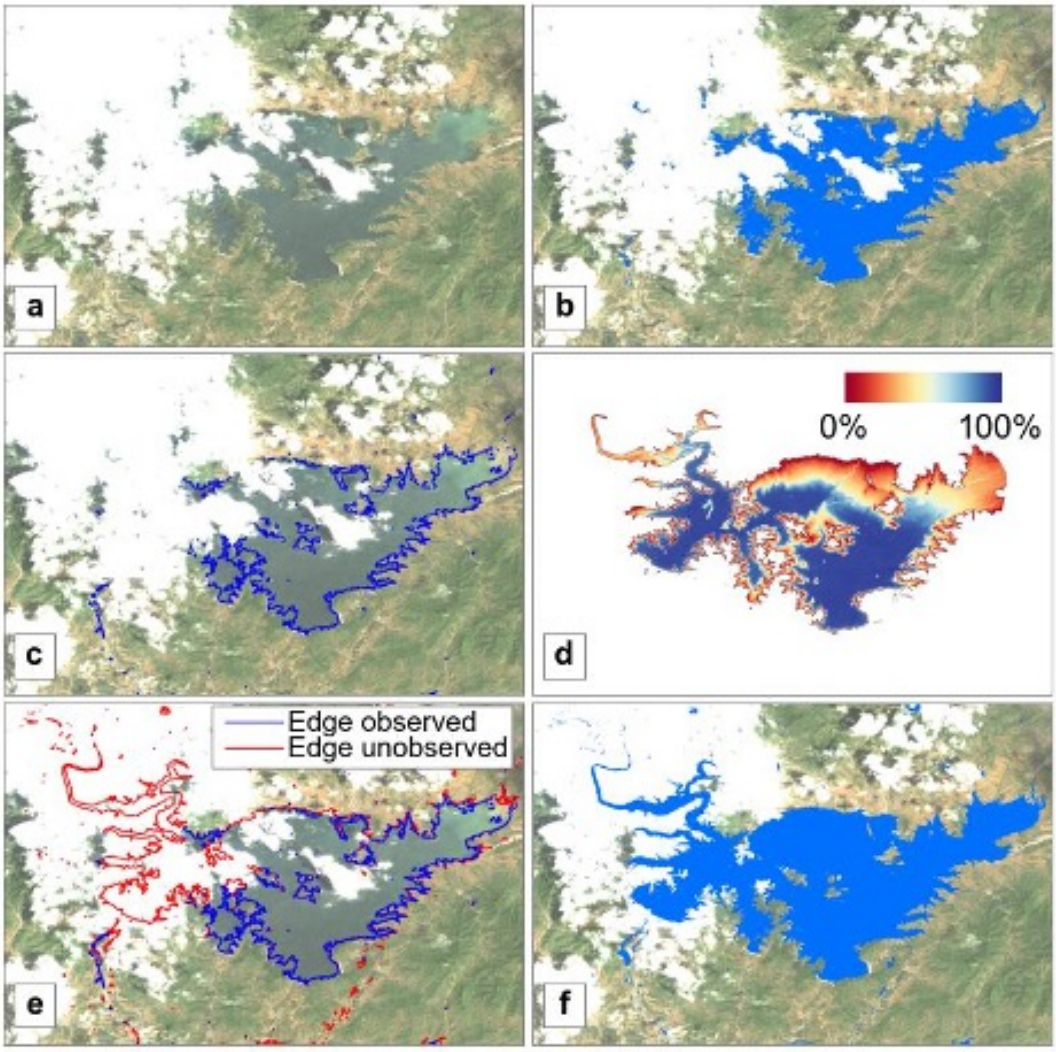

Supplementary Figure 13 | Shown is an example of water area extraction under cloudy conditions. Here using Miyun Reservoir in China as an example, we show (**a**) the Landsat 5 image captured on June 1, 1997, (**b**) the raw water classification from global surface water (GSW) dataset, (**c**) the detected water-land edge, (**d**) the long-term (1984-2020) water occurrence image from the GSW dataset, (**e**) the unobserved edge extended from the observed part, and (**f**) the complete water area.

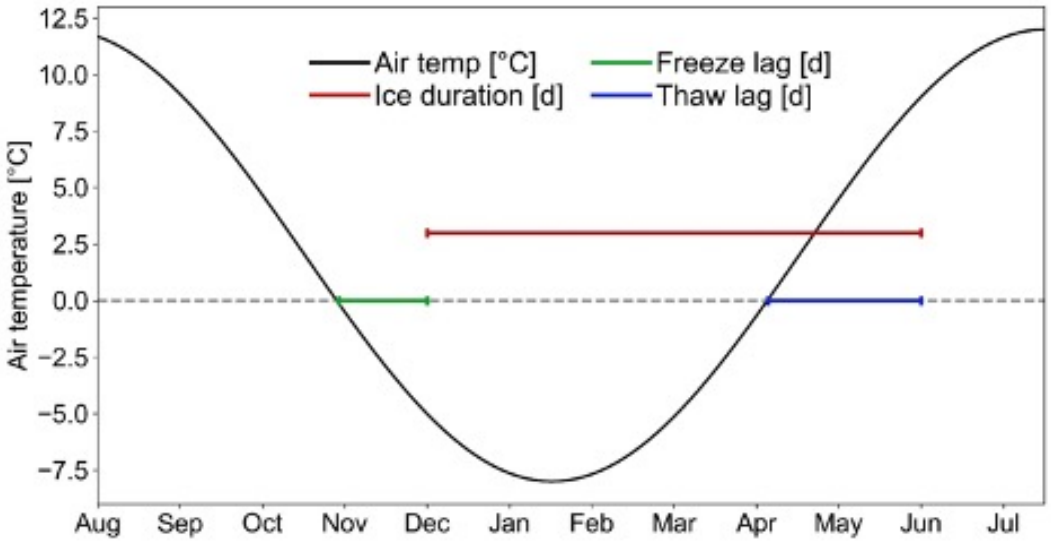

Supplementary Figure 14 | Shown is a conceptual scheme for calculating ice duration based on air temperature. The freeze and thaw lags are calculated following ref. 13 and are equal to 5.815 x $depth^{0.626}$ and -1.003T_{winter} + 21.078 days, respectively, where *depth* is average water body depth in meters and T_{winter} is the average air temperature during the previous winter (Dec, Jan, Feb for the northern hemisphere and Jun, Jul, August for the southern hemisphere)